ELSEVIER

International Journal of Solids and Structures 41 (2004) 2711–2729

INTERNATIONAL JOURNAL OF SOLIDS and STRUCTURES

www.elsevier.com/locate/ijsolstr

Effects of near-tip rotation on pre-buckle crack growth of compressed beams bonded to a rigid substrate

Q.D. Yang [a,*], A.A. Volinsky [b]

[a] *Materials Division, Rockwell Scientific Company, 1049 Camino Dos Rios, Thousand Oaks, CA 91360, USA*
[b] *Department of Mechanical Engineering, University of South Florida, Tampa, FL 33620, USA*

Received 18 February 2003; received in revised form 23 September 2003

Abstract

The macroscopic pre-cracked line scratch test (MPLST), in which a debonded edge of a film is loaded in in-plane compression, has been modeled as a generic, coupled fracture–buckle problem using simple beam theory. Near crack-tip beam rotation (also called root rotation in literature), which always exists due to the eccentric loading in this type of test, has been incorporated into the governing equations. An analytical solution to the augmented problem has been derived. It is found that the near-tip rotation can introduce pre-buckle bending in the film. One important consequence of this pre-buckle bending is that it leads to the reduction of the critical buckling condition. This agrees well with the results of [Int. J. Fract. 113 (2002) 39] obtained by solving the full elastic field near the crack-tip. Furthermore, the pre-buckle bending moment at crack-tip remains negative (leading to crack closure) as long as the pre-buckle crack length is small, but it becomes positive (leading to crack opening) at larger pre-buckle crack length. The negative bending moment causes the crack-tip energy release rate to decrease as the crack propagates, which results in a stable pre-buckle crack growth. Once it becomes positive, however, the bending moment causes crack-tip energy release rate to increase rapidly as crack length increases and hence leads to an unstable (pre-buckle) crack growth. Further, the nominal phase angle is initially larger than the classic prediction of 52.1° owing to the existence of the negative crack-tip bending moment, but it drops quickly upon approaching the buckle point. All these results are confirmed by a rigorous 2D FEM calculation using cohesive zone modeling (CZM) approach. Finally the derived analytical solution has been used to analyze a set of PLST data reported in the literature. It has been demonstrated that plasticity in the adhesive layer and in the bonded film is responsible for the strong *R*-curve toughening characteristics in the deduced interface toughness data. It has also been shown that, once the deduced interface toughness is incorporated into a CZM simulation, both the axial loading and buckling point can be accurately predicted.

Keywords: Fracture; Near-tip rotation; Cohesive zone model; Energy release rate; Buckle; Plasticity

* Correspondence author. Tel.: +1-805-373-4316; fax: +1-805-373-4017.
E-mail address: qyang@rwsc.com (Q.D. Yang).

0020-7683/$ - see front matter © 2003 Elsevier Ltd. All rights reserved.
doi:10.1016/j.ijsolstr.2003.10.002

1. Introduction

Thin film adhesion to a substrate is one of the key critical design parameters in many high-tech industries such as micro-electronics and magnetic recording industries. Films that adhere well to the substrate are always desired. However, how to measure and quantify the adhesion at the film–substrate interface remains an open research topic. Perhaps the most popular method for thin-film adhesion measurements is the micro-indentation test (Marshall and Evans, 1984; Rossington et al., 1984) and its variations such as scratch tests (Benjamin and Weaver, 1960). The common feature of these tests is to promote interfacial debonding through film buckling using out-of-plane compressive loading techniques (indentation). The adhesion is then inferred from measurements of the lateral crack extension (at interface) and the indentation volume.

More recently, a new testing scheme named micro-wedge indentation test for thin-film adhesion measurements has been proposed by De Boer and Gerberich (1996a,b). However, it was found that this test configuration often suffers from film/substrate cracking instead of the desired interface cracking between the film and substrate. Therefore, a modified scheme called pre-cracked line scratch test (PLST) was proposed (De Boer et al., 1997). In such a test, a pre-existing interfacial crack was introduced initially and the film end was then subjected to axial compression, as illustrated in Fig. 1. In this type of tests, typically two fracture configurations will occur, i.e., a usually stable pre-buckle crack extension, and an unstable (usually dynamic) post-buckle crack propagation before it is arrested finally. The mechanics for post-buckle crack propagation and arrest has been extensively studied and is well understood. A general analytical framework based on classic beam theory has been developed for analyzing these types of tests. A detailed review of this framework and its applications has been given by Hutchinson and Suo (1992).

Pre-buckle crack growth, however, has received little attention in the literature, most probably because it is regarded as a simple problem. Applying the above framework to the pre-buckle fracture of bonded beams yields a simple relationship between crack-tip energy release rate and the applied axial load, given in the following equation

$$\mathscr{G} = P^2/2\widehat{E}h, \tag{1a}$$

where $P = \sigma h$ is the in-plane compressive load, and $\widehat{E} = E/(1-\nu^2)$ is the plane strain modulus. Eq. (1a) shows that the energy release rate, $\mathscr{G}$, is independent of crack length. Furthermore, the phase angle, Ψ, in this particular case is also crack length independent ($\Psi = 52.1^\circ$ for a thin beam bonded to a thick rigid substrate). Therefore, according to this theory, when the in-plane stress reaches a critical value so that $\mathscr{G}$ reaches the interfacial joint toughness, Γ_i, crack propagation occurs. As the crack reaches a critical length given by Eq. (1b), the film buckles

$$l_{bkl} = 2\pi\sqrt{\widehat{E}I/P}. \tag{1b}$$

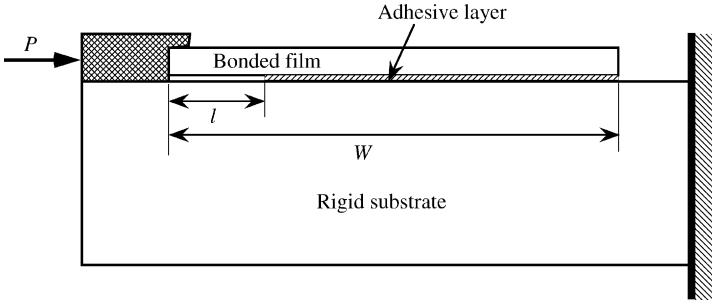

Fig. 1. Experimental setup for a PLST test specimen.

Since both $\mathcal{G}$ and Ψ are independent of the crack length, once a pre-buckle crack starts to grow, it should propagate in an unstable fashion. However, this is inconsistent with experimental observations in many PLST tests (De Boer and Gerberich, 1996a,b). More recently, a macroscopic version of the pre-cracked line scratch test (PLST) by Volinsky et al. (1999) (Fig. 1) also clearly demonstrated stable crack propagation with increasing edge loading before the film buckled.

These observations strongly suggest that the classic solution of this problem should be carefully re-examined. Two key assumptions are associated with the above analysis. One is that the crack length is much longer than the thickness of the bonded beam, so that simple beam theory applies. The other core assumption is that the beam section at crack-tip is clamped (zero near-tip rotation). Provided these assumptions are satisfied, the energy release rate and phase angle can be explicitly expressed by axial force and bending moment acting at the crack tip. It is seen in Eq. (1a) that there is no bending term, i.e., pre-buckle bending is neglected. This was not true in Volinsky et al.'s (1999) macroscopic PLST test, where a considerable amount of pre-buckle bending was observed accompanying stable pre-buckle crack extension. It is noted that the macroscopic PLST test proposed by Volinsky et al. (1999) is very appealing for thin film adhesion test because it can explore both the pre-buckle and post-buckle fracture behavior in a single test. However, the concerns described above need to be addressed before it can be used as a standardized testing scheme.

One possible explanation is the rotation of the beam near the crack-tip that may occur due to the existence of a finite-sized fracture zone ahead of the crack-tip and loading eccentricity. This near tip rotation has also been called root rotation in literature (Kim and Avaras, 1988; Kinlock et al., 1994). It has been found that the near-tip rotation effects are important to many fracture problems such as double cantilever beams (DCB) under transverse point loading (Kanninen, 1973; Williams, 1989, 1995). A recent investigation of near-tip rotation effects by Li et al. (2004) concluded that, while in general it should not be taken as the origin of correction factor for energy release rate, near-tip rotation does become important if it causes a sufficiently large change in geometry that affects the appropriate calculation of crack-tip forces and moments. This could very well be the case for the pre-buckle fracture of a compressed beam shown in Fig. 1. Although the beam is nominally axially loaded, the fact that the applied axial load is balanced by the interfacial shear stress in the fracture zone ahead of the crack-tip will inevitably introduce some degree of loading eccentricity, as illustrated in Fig. 2. This loading eccentricity tends to induce near-tip rotation, which in turn would induce additional bending moment and shear force in the beam. These additional loads, which are neglected in Eq. (1a), may become important when the axial load is sufficiently large. It is one of the purposes of this study to examine the effects caused by the near-tip rotation.

In this study, the PLST test configuration will be modeled as a generic coupled fracture–buckle problem shown in Fig. 2. Near-tip rotation will be introduced into the basic governing equations of beam theory to allow for pre-buckle bending. Analytical solutions will be derived and the effects of near-tip rotation on buckling condition, energy release rate and phase angle calculations will be explored in detail. Furthermore,

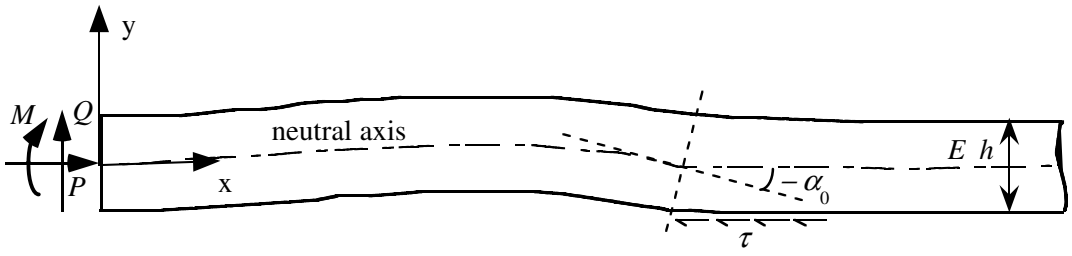

Fig. 2. Schematic draw of the problem analyzed. The axial load, bending moment, and shear force point to their positive senses.

a rigorous 2D FEM analysis using a cohesive zone model (CZM) representing the interface between a bonded beam and a substrate will be carried out to further validate the augmented beam theory predictions.

2. Equations and solutions

The problem to be solved is illustrated in Fig. 2, where the left end of the compressed beam is clamped, and the axial compressive load is balanced by the interface shear stress ahead of the crack-tip. The effective loads depicted in Fig. 2 also define their positive sense. It can be easily shown from a local stress equilibrium analysis at the crack-tip that the interfacial shear stress introduces local bending that leads to the near-tip rotation illustrated in Fig. 2. Since the left end is clamped, this tendency of rotation leads to a bending moment and a transverse shear force acting on the edge, in addition to the applied axial compressive force. Therefore, the fracture–buckle problem can be described as following (Timoshenko and Gere, 1961)

$$\begin{aligned} &\widehat{E}I\frac{\mathrm{d}^4v(x)}{\mathrm{d}x^4}+P\frac{\mathrm{d}^2v(x)}{\mathrm{d}x^2}=0,\\ &v(x)|_{x=0}=\left.\frac{\mathrm{d}v(x)}{\mathrm{d}x}\right|_{x=0}=0,\\ &v(x)|_{x=l}=0,\quad \left.\frac{\mathrm{d}v(x)}{\mathrm{d}x}\right|_{x=l}=-\alpha_0, \end{aligned} \tag{2a}$$

where $v(x)$ is the deflection function, l is the current crack length, and α_0 is the crack tip rotation angle. A normalized form of the above equations is

$$\begin{aligned} &\frac{\mathrm{d}^4V(X)}{\mathrm{d}X^4}+K^2\frac{\mathrm{d}^2V(X)}{\mathrm{d}X^2}=0,\\ &V(X)|_{X=0}=\left.\frac{\mathrm{d}V(X)}{\mathrm{d}X}\right|_{X=0}=0,\\ &V(X)|_{X=L}=0,\quad \left.\frac{\mathrm{d}V(X)}{\mathrm{d}X}\right|_{X=L}=-\alpha_0, \end{aligned} \tag{2b}$$

where the normalization is defined as

$$K^2=Ph^2/\widehat{E}I;\quad V(X)=v(x)/h;\quad X=x/h;\quad L=l/h. \tag{2c}$$

The solution to Eq. (2b) is

$$V(X)=-\frac{\alpha_0}{K}\frac{\{K(L-X)-KL\cos[KX]+KX\cos[KL]+\sin[KX]+\sin[K(L-X)]-\sin(KL)\}}{KL\sin[KL]+2\cos[KL]-2}. \tag{3a}$$

The bending moment and shear force in the beam as functions of X are

$$M(X)=\frac{\mathrm{d}^2V(X)}{\mathrm{d}X^2}=-\frac{K\alpha_0\{KL\cos[KX]-\sin[KX]-\sin[K(L-X)]\}}{KL\sin[KL]+2\cos[KL]-2}, \tag{3b}$$

$$Q(X)=\frac{\mathrm{d}^3V(X)}{\mathrm{d}X^3}+K^2\frac{\mathrm{d}V(X)}{\mathrm{d}X}=\frac{K^2\alpha_0\sin(KL/2)}{KL\cos(KL/2)-2\sin(KL/2)}, \tag{3c}$$

respectively.

In the above derivation, the crack tip rotation is included as an "independent" variable to show how it influences the calculation of crack tip effective forces and bending moment. However, as pointed out by

Li et al. (2004), it is important to appreciate the crack tip rotation is a combined effect caused by crack-tip bending moment, $M(L)$, shear force, $Q(L)$, and axial load, K^2. Dimensional considerations show that the crack-tip rotation has the following form

$$\alpha_0 = \frac{C_m M(L) + C_p K^2 + C_q Q(L)}{12}, \tag{4}$$

where C_m, C_p, and C_q are functions of elastic constants and geometry. Li et al. (2004) carried out a systematic investigation using rigorous FEM to determine the three coefficients as functions of elastic constants and geometric parameters. For beams bonded to a rigid substrate, it was found that $C_m \cong 4.5$, and $C_p \cong C_q \cong 2.0$ (Li et al., 2004). Note that each of the three values is the smallest possible among all the materials combinations and geometries.

The crack-tip bending moment and shear force, $M(L)$ and $Q(L)$, can be obtained from Eqs. (3b) and (3c)

$$M(L) = f_m \alpha_0, \tag{5a}$$

$$Q(L) = f_q \alpha_0, \tag{5b}$$

where

$$\begin{aligned} f_m &= -\frac{K[KL\cos(KL) - \sin(KL)]}{KL\sin(KL) + 2\cos(KL) - 2}, \\ f_q &= \frac{K^2 \sin(KL/2)}{KL\cos(KL/2) - 2\sin(KL/2)}. \end{aligned} \tag{5c}$$

The near-tip rotation angle can therefore be determined by substituting Eq. (5) into Eq. (4), which gives

$$\alpha_0 = \frac{C_p K^2}{12 - C_m f_m - C_q f_q}. \tag{6}$$

The full solution to Eq. (2) is achieved by substituting Eq. (6) into Eqs. (3a)–(3c).

Now α_0 is uniquely determined by the axial load and crack length. Further, the crack-tip bending moment and shear force are also known once α_0 is determined. Together with the applied axial load, the crack tip energy release rate can be computed. For the beam-like geometry shown in Fig. 1, Suo and Hutchinson (1990) have shown that the crack-tip energy release rate can be calculated from the effective bending moment and axial force at crack-tip, irrespective to how they vary behind the crack-tip. A good and insightful example is a double cantilever beam (DCB) under symmetric remote point loading, while the crack-tip bending moment changes constantly with crack length, the energy release rate can always be calculated using Eq. (7) (without axial load contribution) with crack-tip bending moment being the product of the load and the instant crack length. More recently, Li et al. (2004) have also demonstrated that the same is true for shear force. As will be shown later, shear force has very little contribution to the energy release rate, compared to the axial compression and bending. Therefore, in the following energy release rate calculations, only contributions from crack-tip bending moment and axial force are included. The normalized total energy release rate is, according to Suo and Hutchinson (1990)

$$\overline{\mathscr{G}}(L) = \frac{\mathscr{G}h^2}{\widehat{E}I} = \frac{M(L)^2}{2} + \frac{(K^2\cos\alpha_0)^2}{24}. \tag{7}$$

One can further partition the energy release rate into nominal modes I and II using the concept of stress intensity factors (SIF), following Thouless et al. (1987)

$$\begin{aligned}\overline{\kappa}_{\mathrm{I}} &= \frac{\kappa_{\mathrm{I}} h^{5/2}}{\widehat{E}I} = \sqrt{(K^2\cos\alpha_0)^2/2 + 6M^2}\cos(\omega-\beta),\\ \overline{\kappa}_{\mathrm{II}} &= \frac{\kappa_{\mathrm{II}} h^{5/2}}{\widehat{E}I} = \sqrt{(K^2\cos\alpha_0)^2/2 + 6M^2}\sin(\omega-\beta),\\ \beta &= \tan^{-1}\left[2\sqrt{3}M/(K^2\cos\alpha_0)\right],\end{aligned} \tag{8}$$

where $\overline{\kappa}_{\mathrm{I}}$ and $\overline{\kappa}_{\mathrm{II}}$ are the normalized modes I and II SIF, and ω is the phase factor, which in this case (beams bonded to a rigid substrate) is 52.1°. Therefore, the phase angle is

$$\psi = \tan^{-1}(\overline{\kappa}_{\mathrm{II}}/\overline{\kappa}_{\mathrm{I}}) = \omega - \beta.^{1} \tag{9}$$

3. Results of beam theory with near-tip rotation

3.1. Buckling condition with near-tip rotation

The buckling condition for an axially compressed beam assuming clamped condition at crack-tip (zero near-tip rotation) is given by Eq. (1b), which in the normalized form is

$$(KL)_{bkl} = 2\pi. \tag{10}$$

This condition can also be derived by setting the denominator of Eq. (3a) to be zero and solving for (KL), assuming α_0 is a finite constant. However, as shown by Eq. (6), α_0 itself is a function of axial load and crack length. Fig. 3 shows crack tip rotation angle (in radians) as a function of crack length for four different loading levels. It is seen that α_0 is an increasing function of both axial load, K, and crack length, L. More importantly, for a fixed K, α_0 increases sharply to infinity when L approaches a certain point, indicating that a buckling condition is reached. At this point, the beam deflection and bending moment also approach infinity (Eq. (3)).

The buckling point can be found by searching for the smallest root of the following equations (i.e., by setting the denominator of Eq. (3a) or (3b) to be zero)

$$KL\sin(KL) + 2\cos(KL) - 2 = 0, \tag{11a}$$

or

$$12 + \frac{C_m}{L}\frac{KL[KL\cos(KL) - \sin(KL)]}{KL\sin(KL) + 2\cos(KL) - 2} - \frac{C_q}{L^2}\frac{(KL)^2\sin(KL/2)}{KL\cos(KL/2) - 2\sin(KL/2)} = 0. \tag{11b}$$

The solution to Eq. (11a) is Eq. (10). The solution to Eq. (11b), unfortunately, cannot be obtained analytically. However, it can be readily seen that $(KL)_{bkl}$ is no longer independent of crack length. Fig. 4 depicts the relation between $(KL)_{bkl}$ and L. The buckling condition without near-tip rotation correction, i.e., $(KL)_{bkl} = 2\pi$, is also shown for comparison. With near-tip rotation correction, $(KL)_{bkl}$ is a weakly increasing function of crack length. The corrected $(KL)_{bkl}$ is always smaller than the classic solution of 2π, but asymptotically approaches 2π when L increases. The deviation from 2π is larger for shorter cracks because shorter beams require larger Ks to buckle, which in turn induces larger near-tip rotation (Fig. 3).

It is of interest to note that, owing to the existence near-tip rotation, the buckling condition is always smaller than the Euler buckling condition. The reduction of $(KL)_{bkl}$ is small in this study. However, it should be noted that the near-tip rotation remains small in this study due to the particular loading and geometry of the PLST configuration (Fig. 2). The near-tip rotation could be much larger for other

[1] In the calculation of phase angle, the reference length chosen here is the beam thickness, h.

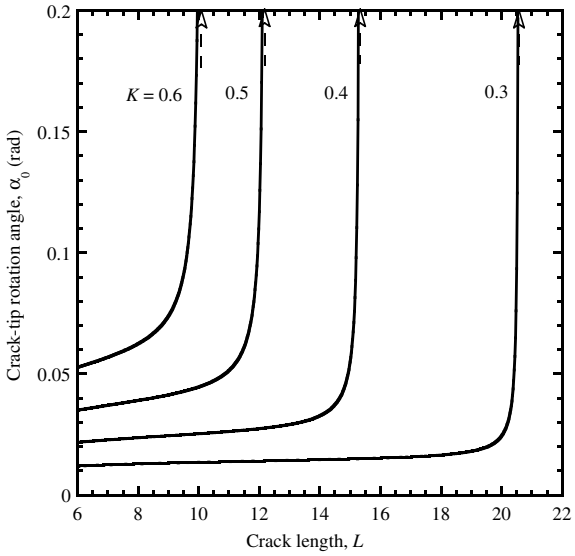

Fig. 3. Crack tip rotation angle (in radians) as functions of crack length for four different loading levels. Dashed line with arrowhead pointing to the buckling point for each load.

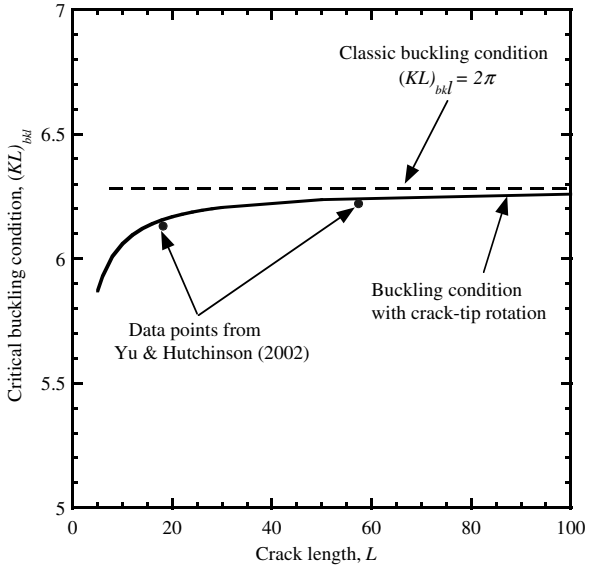

Fig. 4. Buckling condition with near-tip rotation correction compared with the classic prediction assuming clamped condition at crack-tip. The two data points are from Yu and Hutchinson (2002).

geometries. For example, the near-tip rotation effects may be much greater if the substrate is much more compliant than the beam. Yu and Hutchinson (2002) recently studied the influence of substrate compliance on buckling delamination of thin films. They used an integral equation formulation from elasticity to account for the near tip deformation field (so that any near-tip rotation is implicitly included). They found that substrate compliance does reduce the critical buckling condition. Even if the substrate is rigid,

reduction of buckling condition persists due to the 2D near-tip deformation of the bonded beam. Two data points extracted from that study are shown in Fig. 4. It is very encouraging that the augmented beam theory with near-tip rotation consideration does an excellent job in capturing the reduction of buckling condition. A full investigation to determine whether the augmented beam theory can fully account for both the geometry and the elastic modulus mismatch between substrate and bonded beams/films is under way.

3.2. Pre-buckle bending moment and shear force

Fig. 5 shows the normalized crack-tip bending moment (Fig. 5a) and shear force (Fig. 5b) as functions of crack length. Fig. 5a shows that for each case, the bending moment at crack initiation ($L = 6$) is always

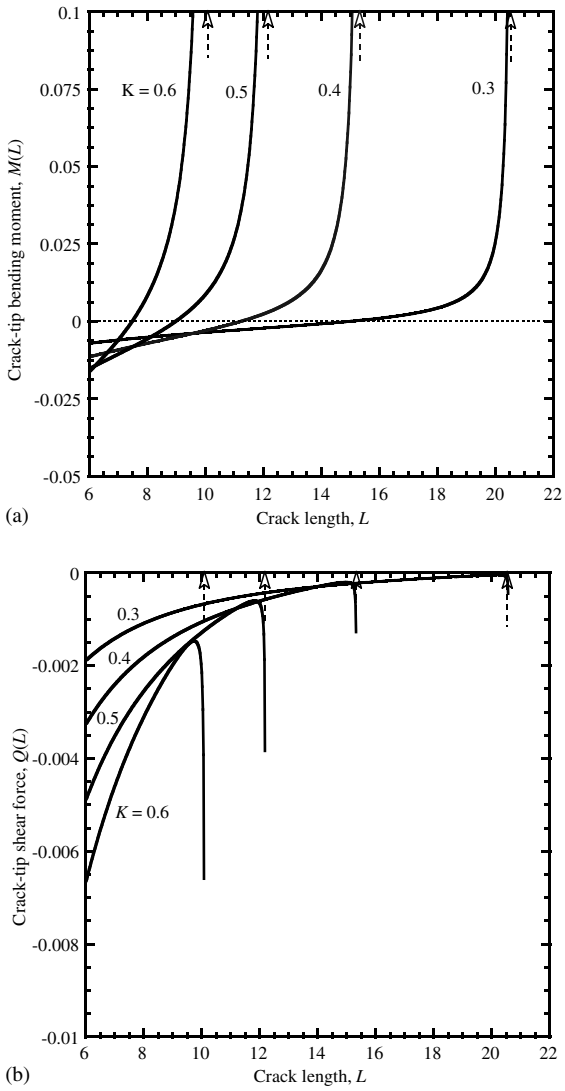

Fig. 5. (a) The crack tip bending moment and (b) the shear force, as functions of crack length. Dashed line with arrowhead pointing to the buckling point for each load.

negative (leads to crack closure). As the crack propagates, the bending moment approaches zero and eventually becomes positive (leading to crack opening). As will be demonstrated later, the (initial) negative bending moment is a key element in understanding stable pre-buckle crack growth usually seen in the PLST test. Once it enters the positive territory, the bending moment increases quickly as crack length further increases and becomes infinite at the buckling point. The point at which the bending moment changes sign can be found by searching for the zero point of the numerator in the function f_m of Eq. (5a), that is, $KL\cos(KL) - \sin(KL) = 0$. This gives

$$KL \cong 4.49. \tag{12}$$

It is interesting to note that Eq. (12) is actually the buckling condition for a beam that is clamped at one end and pinned (free to rotate) at the other. This is one of the two limits that bound the buckling conditions with near-tip rotation modification. The other limit is given by Eq. (10), which is the buckling condition of a beam clamped at both ends.

The evolution of the crack-tip bending moment from negative to positive during pre-buckle crack growth can also be elucidated by the following equation [2]

$$M(L) = M(0) + Q(0) \cdot L, \tag{13}$$

where $M(0)$ and $Q(0)$ are the bending moment and shear force exerted by the clamped end, respectively. $M(0)$ is positive and must be an increasing function of L because larger L introduces larger beam (pre-buckle) deflection, which in turn requires a larger bending moment to maintain the rotation-free boundary condition at the clamped end. The shear force $Q(L)$ is a constant throughout the cracked beam (Eq. (3c)). Furthermore, as shown in Fig. 5b, the shear force is negative and its magnitude decreases as L increases (except near the very vicinity of buckling point, where the shear force approaches negative infinity due to an infinitely large near-tip rotation (cf. Eq. (5b)). At small L, the negative $Q(0) \cdot L$ term overcomes the positive $M(0)$ and hence $M(L)$ is negative. The opposite holds when L becomes sufficiently large.

It is noted that the magnitude of the shear force (Fig. 5b) is always negligibly small compared to the bending moment (Fig. 5a) or the axial load (K^2). Therefore, its direct contribution to the total energy release rate at crack-tip, $(1+v)Q(L)^2/5$ (with v being the Poisson's ratio of the beam), must also be small. This is clear from Fig. 6, which plots the individual contribution to crack-tip energy release rate from axial load, bending moment, and shear force. The contribution from shear force is indeed negligibly small. However, this should NOT be misinterpreted as implying that the shear force is not important in the current study. The shear force is indeed a very important element in the current analysis. First, it affects the crack-tip energy release rate calculation through the effective crack-tip bending moment (Eq. (13)). Second, it is needed to satisfy the boundary condition of $V(0) = 0$. If the shear force were to be neglected, the clamped condition would become a (shear) stress-free condition at $X = 0$, with the Euler buckling condition (without near-tip rotation correction) $(KL)_{bkl} = \pi/2$. The solution to that problem (without near-tip rotation consideration) has been explored by Chiu et al. (1998) to analyze the chipping of brittle materials.

Finally, Fig. 6 also shows that, while the energy release rate from the axial load, $(K^2\cos\alpha_0)^2/24$, stays constant almost up to the buckling point; the bending contribution comes into play much earlier, typically when about 90% of the buckling condition is reached. Once bending is important, the crack growth becomes unstable until it passes through the buckling point, as discussed below.

[2] It can be readily shown that $M(L)$ calculated from Eq. (13) is identical with that obtained from Eq. (3b).

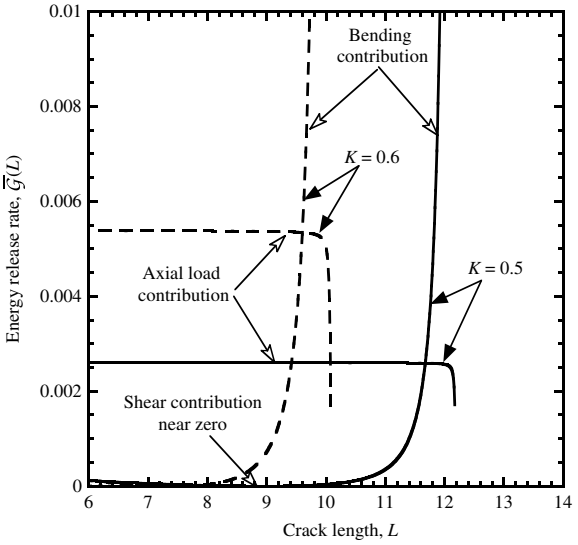

Fig. 6. Individual contributions to energy release rate from the axial load, pre-buckle bending, and shear force.

3.3. Energy release rate and phase angle

The total energy release rate at the crack-tip is shown in Fig. 7a for four different loading levels. For all the cases, the crack-tip energy release rate at small crack lengths (when $M(L) < 0$) decreases as the crack grows, because the contribution to $\mathcal{G}$ from the bending decreases as $M(L) \to 0$ from the negative side (Fig. 6). However, once $M(L)$ becomes positive, the energy release rate increases quickly as the crack length increases. This is an unstable crack growth condition in a load-controlled test, which may cause difficulty in identifying the exact buckling point in such a test. The drop of $\overline{\mathcal{G}}$ is more significant at larger K values than smaller Ks. This indicates that a stronger interface bonding, which requires larger K to propagate the crack, the negative crack-tip bending moment introduces greater influence on stabilizing the crack growth at smaller crack length. If the interface bonding is very weak such that only a very small K is needed to propagate the crack, near-tip rotation is thus small and has little influence on stabilizing the crack propagation. This can be seen from the case of $K = 0.3$ shown in Fig. 6, which basically recovers Eq. (1) during the pre-buckle crack growth.

The existence of a pre-buckle bending moment also significantly alters the classic picture of the mode mixedness calculation. Fig. 7b shows the variation of phase angle as a function of crack length for four different loading levels. The upper dashed line indicates the classic solution of 52.1°. The phase angles differ quite dramatically from the classic solution. The phase angle at crack initiation is always larger than 52.1°, owing to the negative bending moment (Fig. 5a), and drops steadily as crack grows when the bending moments approaches zero from negative territory. Once passing the turning point given by Eq. (12), however, $\psi(L)$ drops rapidly with further crack growth because the rapidly increasing positive bending moment dominates the fracture process (Fig. 6). In the limit of $L \to L_{bkl}$, it is seen that $M(L) \to +\infty$, and $\psi(L) \to -37.9°$, which is the classic solution of crack growth due to pure bending moment (Thouless, 1990). It is noted here that the near-tip rotation angles associated with the four loading levels in Fig. 7 are given in Fig. 3. Note the initial pre-buckle rotations are indeed fairly small, far less than 0.1 rad (5.7°), yet they make significant difference in the energy release rate and phase angle calculations, compared to the classic beam theory without near-tip rotation correction.

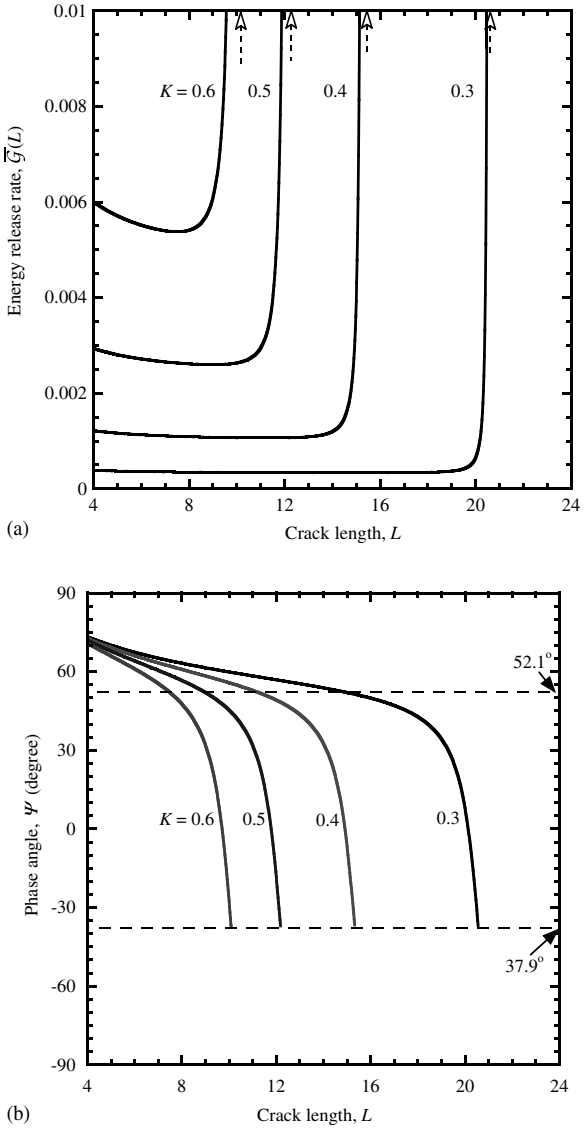

Fig. 7. (a) Crack tip energy release rate and (b) phase angle for four different axial loading levels. Dashed line with arrowhead pointing to the buckling point for each load.

Finally, if the joint toughness Γ_i is known, one can calculate the axial compressive load required to drive the pre-buckle crack using Eq. (7). Fig. 8 gives the results of such a calculation. At small crack length, an increasing loading parameter, K, is needed to drive a crack, which indicates a physically stable crack growth, as observed in the PLST tests. This is a direct effect of negative bending moment that occurs at the small crack length, because it causes the energy release rate to decrease (Fig. 7a). When the bending moment becomes positive, however, the required K drops rapidly until the beam buckles.

The decrease of $\overline{\mathcal{G}}(L)$ in Fig. 7a, (or, equivalently, the increase of $K(L)$ in Fig. 8) at smaller L appears not very sensitive to L—seems not enough to ensure a stable crack growth in a real test. However, it should be appreciated that the case studied here is a limiting case: an elastic (compliant) beam bonded to an infinitely

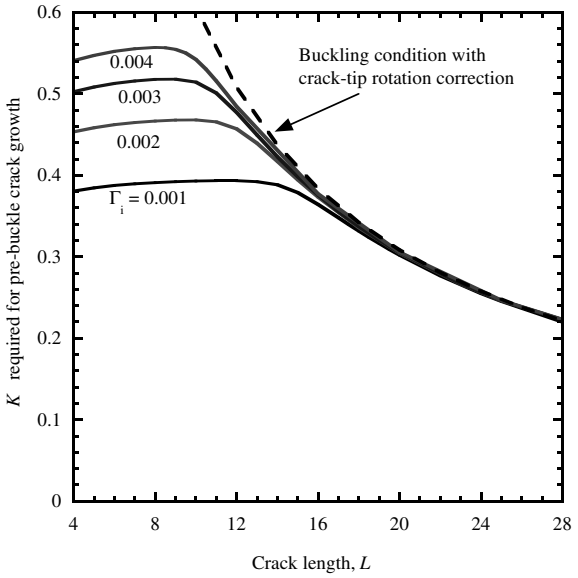

Fig. 8. Axial loading parameter K required for crack extension for four different interfacial toughness values.

thick and rigid substrate. The crack-tip rotation in the beam is among the smallest possible compared to other geometry and material combinations (Li et al., 2004). Not surprisingly the results are among the least deviation from the classic solutions. Nonetheless, one can still see the increasingly stable configuration ($\overline{\mathscr{G}}(L)$ drops much more and much quicker) as axial loading parameters increases (equivalent to increasingly large joint toughness in Fig. 8). In general crack-tip rotation angle is a function of the two Dundur's parameters (elastic moduli mismatch), the thickness ratio of the two bonded substrates, and the joint toughness (Li et al., 2004). The near-tip rotation effects are expected to be much more significant for other geometry and material combinations. A detailed full-scope parameter study of such problems is under way and will appear elsewhere.

3.4. Implications to macroscopic pre-cracked line scratch test

Eqs. (7) and (9) constitute the key of interpreting experimental results from a PLST. In a PLST, typically the applied load (P) and crack length (l) are recorded as functions of time (e.g., Volinsky et al., 1999). This can readily be converted to the normalized K–L curve, from which the interface toughness and phase angle as functions of crack length can be readily computed using these equations. A lot useful information can be included in such results. Firstly, joint toughness as a function of phase angle can be conveniently obtained through one single test for a relatively large range of phase angles (ψ). Theoretically $\psi(L)$ approaches 90° as L decreases to zero, which means the possible range of $\psi(L)$ can be from −37.9° to 90° in a single PLST. This is the most appealing feature of PLST. Secondly, the calculated joint toughness may contain extra information such as R-curve toughening effects. R-curve phenomenon usually accompanies the gradual development of crack-tip plasticity in the beam as crack advances. Any such information will be necessarily included in the measured K–L curve and will be retained in the calculated joint toughness. [3]

[3] This works only under the condition that the crack-tip plastic zone size is small compared to the beam thickness (small-scale yielding). Otherwise, the elasticity based beam theory used in this study is violated and one has to seek other means such as cohesive zone model with elasto-plastic material model for the beam (e.g., Yang and Thouless, 2001) to back out the R-curve toughening effects.

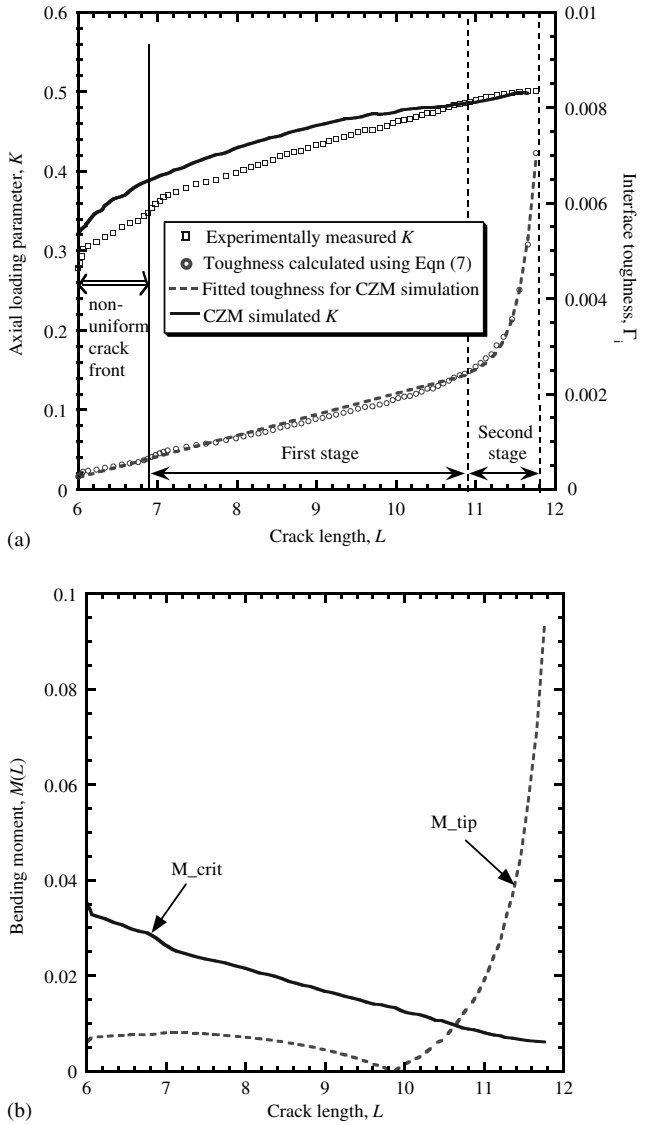

Fig. 9. (a) Experimentally measured K–L data (□) by Volinsky et al. (1999) and the deduced interface toughness (◯) using Eq. (7). The dashed line is the fitted toughness curve for CZM simulation and the solid line is the CZM predicted K–L curve based on the fitted toughness. (b) Critical bending moment at crack-tip for plasticity to occur in the bonded film as function of crack length (solid line), deduced from the measured K–L data using Eq. (14b), and the actual crack-tip bending moment deduced from the measured K–L data using Eq. (3) (dashed line).

Fig. 9 gives such an example making use of the data reported in Volinsky et al. (1999). In this test, a Polycarbonate (PC) film of 100 mm long, 1.7 mm thick and 18 mm wide was bonded to a very thick piece of steel substrate, by a thin layer (~0.1 mm thick) of cyanoacrylate. The testing rig is illustrated in Fig. 1. The original data of axial load as a function of crack length was normalized and shown as a K–L curve (Eqs. (2c) and (7)) in Fig. 9a (left-hand Y-axis). Note that in this test the crack front during the initiation stage ($L < 6.8$) was not uniform across the film width. The toughness calculation in that region is therefore inaccurate. Despite that, it is seen that the loading parameter K increased continuously until the onset of

dynamic crack growth (buckling) occurred when L reached about 11.8, indicating that some degree of R-curve toughening effect set in during the pre-buckle crack propagation. The computed interface toughness (Γ_i) as a function of L is also plotted in the same figure (right-hand Y-axis). Note that the R-curve effect helped to maintain a stable (pre-buckle) crack growth up to the buckling point, because the ever-increasing interface toughness required the applied K be constantly increased. It is interesting to see that while the K is a near-linear function of L, $\Gamma_i(L)$ clearly shows two very distinct stages of L-dependence: in the earlier crack growth stage ($L < 10.88$), $\Gamma_i(L)$ is almost a linear function; however, Γ_i increases exponentially thereafter until buckling point is reached.

While the linear L-dependence of Γ_i can be explained by the plastic zone development confined in the adhesive (cyanoacrylate) layer, as did in Volinsky et al. (1999), the rapid (nonlinear) increase of Γ_i in the second stage defies this explanation because the exponential increase of Γ_i is accompanied by a level-off of the applied load (Fig. 9a). A close examination of the stress state in the film reveals that the plastic deformation *in the film* near the crack-tip region is responsible for the unusually strong R-curve effect. According to elasto-plastic theory, plastic deformation in the film will occur when the stress at the outmost layer ($y = \pm h/2$) reaches the yield stress of the film, σ_y. Note that for a compressed film, the total stress is the sum of axial compression stress, $P\cos\alpha/h$, and bending stress, my/I. It follows that the maximum stress (compression) is

$$\sigma_{\max} = \frac{|m| \cdot (h/2)}{I} + \frac{P\cos\alpha}{h}, \tag{14a}$$

where $|m|$ is the absolute value of un-normalized crack-tip bending moment. The elastic limit of the film deformation, $\sigma_{\max} \leqslant \sigma_y$, gives the critical bending moment, $M_$crit, above which plasticity in the film will occur [4] (in normalized form)

$$M\_\text{crit} = 2\sigma_y/\widehat{E} - K^2\cos\alpha/6. \tag{14b}$$

Comparing the crack-tip bending moment, $M(L)$, against the critical bending moment, one can estimate when the plasticity occurs. Such a comparison is shown in Fig. 9b, where the critical bending moment, $M_$crit, and the absolute value of crack-tip bending moment, $M_$tip, both calculated from the measured data of Volinsky et al. (1999), are plotted. The yield stress and plane strain modulus of PC were taken to be 60 MPa and 2.5 GPa, respectively. It is immediately seen that $M_$tip is smaller than $M_$crit when crack length L is less than about 10.7, suggesting no plasticity in the film around the crack-tip. However, $M_$tip exceeds $M_$crit in an exponential fashion as L increases further. The turning point of $L = 10.7$ agrees well with the observed value from the experimental data, $L = 10.88$. This clearly demonstrates that plasticity in the film is responsible for the exponential L-dependence of Γ_i at the second stage in Fig. 9a.

It has been well recognized that plasticity in bonded substrates can cause significant increase of nominal interface toughness, or, work-to-fracture (Wei and Hutchinson, 1997; Yang et al., 2000). For example, Yang et al. (2000) reported an increase of 20 times over the intrinsic mode I joint toughness of a plastically-deforming 90°-peel joint. In viewing of this, the about threefold of increase in Γ_i (from 0.0024 to 0.007) during the second stage in Fig. 9a implies that plasticity in the film is still moderate and this is why the buckling point has not been significantly altered.

[4] For the particular geometry and loading studied in the paper, first yield zone does not occur at the crack-tip ($y = -h/2$). Rather, it occurs at the upper stress-free surface ($y = h/2$) where the maximum compressive stress exists. Therefore it is refer to as "plasticity in the film" rather than "crack-tip plasticity".

4. Numerical confirmation via cohesive zone modeling

The analytical solution derived above is based on simple beam theory that is accurate only for slender beams with small to moderate lateral deflection. However, in a PLST the pre-crack length may not be sufficiently long to ensure the accuracy of simple beam theory. Further, the stress/strain field at crack-tip is a complicated 2D field that could not possibly be fully accounted by any beam theory. The resultant effect of the crack-tip stress/strain field is taken into account in the derivation in terms of the near-tip rotation of the bonded beam. It has been demonstrated in Section 3.1 that it does a good job in predicting the reduction of buckling condition. However, whether it can accurately account for the pre-buckle fracture process remains to be validated.

In this section, a 2D finite element model was built to simulate the coupled fracture–buckle problem stated in Fig. 2. The compressed beam has a thickness of 1.7 mm and an elastic modulus of 2.5 GPa. The rigid substrate is modeled as a fixed boundary line. A cohesive zone model was used to mimic the fracture zone between the beam and the substrate. The CZM employs a mode-independent cohesive law similar to that used by Yang and Thouless (2001). A detailed description of the CZM is given in Appendix A. The parameters for the cohesive law are given in the inset of Fig. 10b. The FEM model includes 15,000 4-node, 4500 3-node plane strain elements, and 2000 cohesive zone elements. It took about 1 h of CPU time (HP C-3600 unix workstation) before the calculation was stopped due to divergence, indicating the buckling condition was reached.

Fig. 10a summarizes the results of the CZM modeling. It shows the deflection profiles and the axial stresses (σ_{11}) at three different stages (displacements magnified by 10 times): (1) near crack initiation; (2) at an intermediate stage when the crack-tip bending moment is near zero; and (3) immediately before buckling (buckling point was taken when the simulation failed to converge). The crack-tip bending moment can be obtained from the axial stress distribution along the beam cross-section at crack-tip by

$$M(L) = -\int_0^h [\sigma_{11}(L,y) - \bar{\sigma}_{11}(L)]y\,\mathrm{d}y, \tag{15}$$

where $\bar{\sigma}_{11}(L) = \frac{1}{h}\int_0^h \sigma_{11}(L,y)\,\mathrm{d}y$ is the average stress at the cross-section. The axial stress field at the crack tips of the three stages shows a transition from a negative bending moment in Fig. 10a_1 ($M(L) \sim -0.007$) to a small positive moment in Fig. 10a_2 ($M(L) \sim +0.031$), and to a large positive bending moment in Fig. 10a_3 ($M(L) \sim +0.090$). This verifies the beam theory prediction at least qualitatively.

The required loading parameter and phase angle as functions of crack length predicted by CZM are shown in Fig. 10b. The corresponding beam theory predictions are included for comparison. The analytical solution captures the essence of CZM results very well, especially the crack length dependence of the applied load and the rapid drop in phase angle as the crack propagates. It is rather satisfactory to see that the loading parameter (K) predicted by the augmented beam theory with near-tip rotation is only 8% lower than that predicted by 2D CZM calculation.

Noted that although the phase angles predicted by the beam theory are very close to CZM predicted values, they should not be compared directly. In beam theory, the calculation of phase angle depends upon a reference length scale, which could be chosen rather arbitrarily (beam thickness, h, is used in Eq. (9)). However, a simple transformation rule exists between different choices of the reference length (Hutchinson and Suo, 1992). In the CZM modeling, the phase angle was calculated from fracture energies associated from the modes I and II fracture processes as defined in Appendix A. This calculation involves a natural length scale—the fracture zone size. Perhaps due to serendipity, the CZM parameters used in this study yielded a fracture zone of a size comparable to the beam thickness (simple estimation from shear lag analysis showed that the CZM fracture zone for this case is 3.5 mm, or, about twice the beam thickness). This is why the two sets of phase angles are so close. Had the fracture zone been much different from the beam thickness, a simple transformation would be noted between the phase angle lines in Fig. 10b.

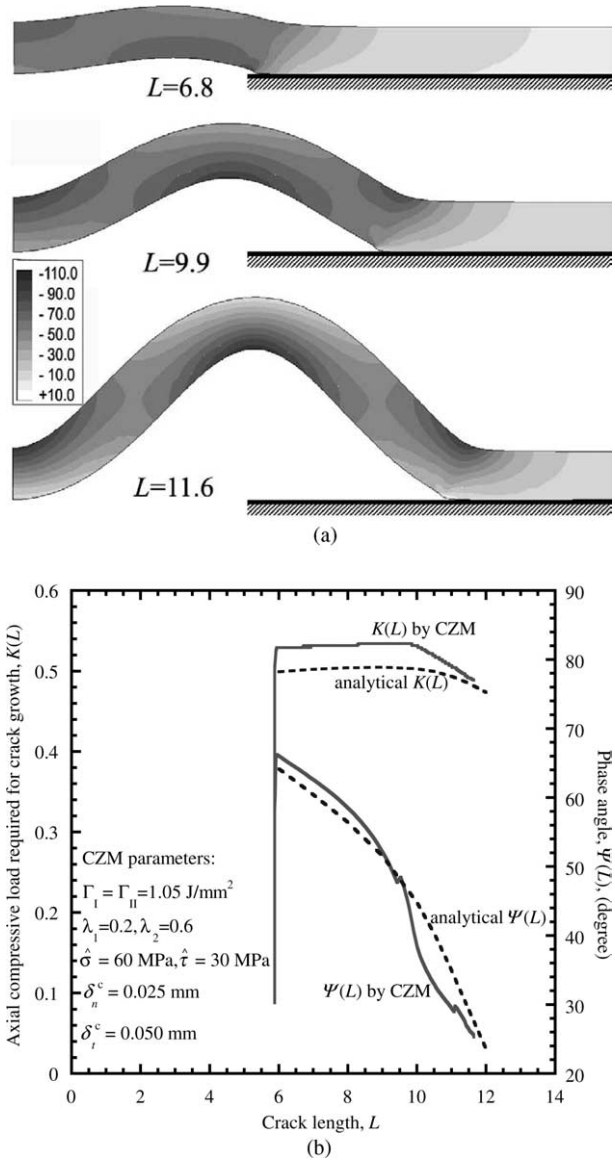

Fig. 10. (a) Axial stress states predicted by CZM at three different pre-buckle crack growth stages, showing crack-tip bending moment evolves from a negative value (a_1) at initiation, to a near zero value at an intermediate stage (a_2), and finally to a positive value immediately before buckle (a_3). Displacements are magnified by a factor of 10. Also shown is the fracture zone size (shear zone size) for the CZM simulation. (b) The CZM predicted loading parameter (K) and phase angle (ψ) as functions of crack length (L), compared to the corresponding analytical results (dashed lines).

Finally, for completeness purpose, the deduced interface toughness with R-curve effect included (Fig. 9a) was incorporated into a modified cohesive law (mode-independent) to simulate the PLST described in Volinsky et al. (1999). The modified cohesive law has constant cohesive strengths ($\widehat{\sigma} = 60$ MPa and $\widehat{\tau} = 30$ MPa), but the fitted curve of the deduced toughness data (dashed line in Fig. 9a) is taken as the toughness

of the CZ elements. Thus each CZ element has a location-dependent toughness, mimicking the R-curve effect. The fitted curve is represented as

$$\Gamma_i = \begin{cases} 2.0 \times 10^{-4} + 4.4 \times 10^{-4}(L - 5.88) & (5.88 < L \leqslant 10.88), \\ 2.42 \times 10^{-3} + 1.67 \times 10^{-4} \sinh[(L - 10.88)/0.22] & (10.88 < L \leqslant 11.76). \end{cases}$$

It is of interest to see if such a simulation can reproduce the experimentally measured load—crack length data. The computed loading parameter (K—left-hand Y-axis) is superimposed on Fig. 9a (solid line) as a direct comparison to the measured data. Not surprisingly, the simulated K replicates the experimental curve quite accurately—not only the predicted $K(L)$ is sufficiently close to experimental curve, but also the buckling point is captured quite accurately.

5. Conclusions

In this study, the macroscopic pre-cracked line scratch test (MPLST) has been modeled as a generic, coupled fracture–buckle problem using simple beam theory. Near crack-tip beam rotation (also called root rotation in literature), which always exists due to the eccentric loading in this type of test, has been incorporated into the governing equations. An analytical solution to the augmented problem has been derived. It is found that the near-tip rotation can introduce pre-buckle bending in the film. One important consequence of this pre-buckle bending is that it leads to the reduction of critical buckling condition. This agrees well with the results of Yu and Hutchinson (2002) obtained by solving the full elastic field near the crack-tip. Furthermore, it is found that the pre-buckle bending moment at the crack-tip is always negative (leading to crack closure) when the pre-buckle crack length is small, but it becomes positive (leading to crack opening) at larger pre-buckle crack length. The negative bending moment causes the crack-tip energy release rate to decrease as the crack propagates, which results in a stable pre-buckle crack growth. Once it becomes positive, however, the bending moment causes crack-tip energy release rate to increases rapidly as crack length increases and hence leads to an unstable (pre-buckle) crack growth. Furthermore, the nominal phase angle is initially larger than the classic prediction of 52.1° owing to the existence of the negative crack-tip bending moment, but it drops quickly upon approaching the buckle point. All these results are confirmed by a rigorous 2D FEM calculation using a cohesive zone model. Further, the derived analytical solution has been used to analyze a set of PLST data. Interface toughness as a function of crack length has been deduced from the experimental data, which showed strong R-curve effects. Plasticity in the adhesive layer and in the bonded film was found to be responsible for the strong R-curve characteristics. The deduced interface toughness has also been incorporated into a modified cohesive zone model and excellent agreement has been obtained between the CZM predicted and experimentally measured axial load. The CZM also accurately predicted the buckling point of the PLST specimen.

Acknowledgements

The part of work by Q.D. Yang was partially supported by AFOSR grant no. 49620-02-1-006 with Dr. B.L. Lee. The authors would like to acknowledge Drs. B.N. Cox and D.B. Marshall (RSC), and Prof. W.W. Gerberich (Univ. Minnesota) for valuable discussions and critical review of the paper.

Appendix A. A mode-independent cohesive zone model

The mode-independent cohesive law used in this study is a special case of the mixed-mode CZM first used by Yang and Thouless (2001). The model assumes unrelated traction–separation laws for opening and

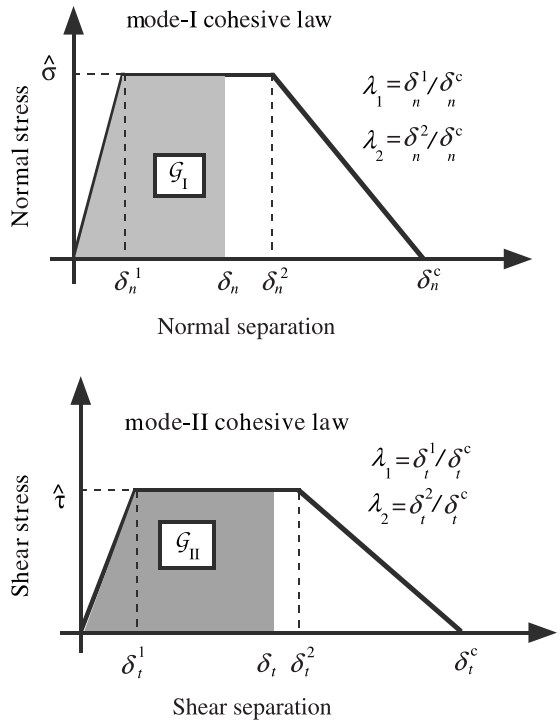

Fig. 11. Schematic illustration of the mixed-mode CZM used in this study. $\mathcal{G}_{\mathrm{I}}$ and $\mathcal{G}_{\mathrm{II}}$ are the modes I and II traction separation energies, at normal and shear displacements of δ_{n} and δ_{t}. $\delta_{\mathrm{n}}^{\mathrm{c}}$ and $\delta_{\mathrm{t}}^{\mathrm{c}}$ are the critical normal and tangential displacements for pure modes I and II fracture.

shear deformation. This is usually appropriate because frequently the modes I and II fracture are due to different failure mechanisms for adhesively bonded structures, and hence, have different traction separation laws. The total traction–separation work absorbed during fracture (frature energy), $\mathcal{G}$, is the sum of the opening (mode I) and shear (mode II) components, $\mathcal{G}_{\mathrm{I}}$ and $\mathcal{G}_{\mathrm{II}}$

$$\mathcal{G} = \mathcal{G}_{\mathrm{I}} + \mathcal{G}_{\mathrm{II}}. \tag{A.1}$$

The two separate components can be calculated by integration of the modes I and II traction–separation curves (Fig. 11)

$$\mathcal{G}_{\mathrm{I}} = \int_0^{\delta_{\mathrm{n}}} \sigma(\delta_{\mathrm{n}})\,\mathrm{d}\delta_{\mathrm{n}}, \qquad \mathcal{G}_{\mathrm{II}} = \int_0^{\delta_{\mathrm{t}}} \tau(\delta_{\mathrm{t}})\,\mathrm{d}\delta_{\mathrm{t}}, \tag{A.2}$$

where δ_{n} and δ_{t} denote the normal and tangential displacements. These are not independent parameters; they evolve together as a natural result of the interplay between the deformation of the adherends and the details of the two traction–separation laws. A failure criterion is required to determine the critical values of the two components of $\mathcal{G}$, $\mathcal{G}_{\mathrm{I}}^*$ and $\mathcal{G}_{\mathrm{II}}^*$, at which separation of the CZM elements occurs. The criterion used in this study is a simple one (Wang and Suo, 1990; Hutchinson and Suo, 1992)

$$\mathcal{G}_{\mathrm{I}}^*/\Gamma_{\mathrm{Io}} + \mathcal{G}_{\mathrm{II}}^*/\Gamma_{\mathrm{IIo}} = 1, \tag{A.3}$$

where Γ_{Io} and Γ_{IIo} are the *total* areas under the opening and shear traction–separation laws, or, the modes I and II fracture toughnesses, respectively.

In such a mixed-mode fracture process, $\mathscr{G}_{\mathrm{I}}$ and $\mathscr{G}_{\mathrm{II}}$ evolve independently as the opening and shear displacements in the cohesive zone develop in response to the applied loads. Once the failure criterion of Eq. (A.3) is met, the normal and shear tractions across the crack plane are assumed to drop to zero instantaneously, and the crack advances. It is seen that the mode-mixedness does not need to be determined specifically in this scheme. Rather, it is an outcome of the numerical calculations, and is dependent on the fracture criteria and traction–separation laws. However, it is often convenient to be able to define it for purposes of comparison. The phase angle is therefore defined as

$$\Psi = \tan^{-1}\left[\left(\frac{\mathscr{G}^*_{\mathrm{II}}}{\mathscr{G}^*_{\mathrm{I}}}\right)^{1/2}\right]. \tag{A.4}$$

This definition is consistency with the standard definition of the phase angle using applied stress-intensity factors (Hutchinson and Suo, 1992).

The mode-independent CZM used in this study is obtained by setting modes I and II fracture toughnesses to be identical, i.e., $\Gamma_{\mathrm{Io}} = \Gamma_{\mathrm{IIo}}$. The shape parameters ($\lambda_1$ and λ_2), which are of only secondary importance, are also set to be identical. However, the peak normal ($\hat{\sigma}$) and shear stresses ($\hat{\tau}$) can be different. So do the critical separation displacements for mode I ($\delta^{\mathrm{c}}_{\mathrm{n}}$) and mode II ($\delta^{\mathrm{c}}_{\mathrm{t}}$).

References

Benjamin, P., Weaver, C., 1960. Measurement of adhesion of thin films. Proc. R. Soc. London, A 254, 163–176.

Chiu, W.C., Thouless, M.D., Endres, W.J., 1998. An analysis of chipping in brittle materials. Int. J. Fract. 90, 287–298.

De Boer, M.P., Gerberich, W.W., 1996a. Microwedge indentation of the thin film fine line—I. Mechanics. Acta Mater. 44, 3169–3175.

De Boer, M.P., Gerberich, W.W., 1996b. Microwedge indentation of the thin film fine line—II. Experiment. Acta Mater. 44, 3177–3187.

De Boer, M.P., Kriese, M., Gerberich, W.W., 1997. Investigation of a new fracture mechanics specimen for thin film adhesion measurement. J. Mater. Res. 12, 2673–2685.

Hutchinson, J.W., Suo, Z., 1992. Mixed mode cracking in layered materials. Adv. Appl. Mech. 29, 63–191.

Kanninen, M.F., 1973. An augmented double cantilever beam model for studying crack propagation and arrest. Int. J. Fract. 9, 83–92.

Kim, K.S., Avaras, N., 1988. Elasto-plastic analysis of the peel test. Int. J. Solids Struct. 24, 417–435.

Kinlock, A.J., Lau, C.C., Williams, J.G., 1994. The peeling of flexible laminates. Int. J. Fract. 66, 45–70.

Li, S., Wang, J.Z., Thouless, M.D., 2004. The effects of shear on delamination of beam-like geometries. J. Mech. Phys. Solids 52, 193–214.

Marshall, D.B., Evans, A.G., 1984. Measurement of adherence of residually stressed thin-films by indentation—I. Mechanics of interface delamination. J. Appl. Phys. 56, 2632–2638.

Rossington, C., Evans, A.G., Marshall, D.B., 1984. Measurement of adherence of residually stressed thin-films by indentation—II. Experiments with ZnO/Si. J. Appl. Phys. 56, 2632–2638.

Suo, Z., Hutchinson, J.W., 1990. Interface crack between two elastic layers. Int. J. Fract. 43, 1–18.

Thouless, M.D., 1990. Fracture of a model interface under mixed-mode loading. Acta Metall. 38, 1135–1140.

Thouless, M.D., Evans, A.G., Ashby, M.F., Hutchinson, J.W., 1987. The edge cracking and spalling of brittle plates. Acta Metall. Mater. 35, 1333–1341.

Timoshenko, S.P., Gere, J.M., 1961. Theory of elastic stability, second ed. McGraw-Hill Publishing Company.

Volinsky, A.A., Nelson, J.C., Gerberich, W.W., 1999. Macroscopic modeling of fine line adhesion tests. Mater. Res. Proc., 563–568.

Wang, J.S., Suo, Z., 1990. Experimental determination of interfacial toughness using Brazil-nut-sandwich. Acta. Metall. 38, 1279–1290.

Wei, Y., Hutchinson, J.W., 1997. Interface strength, work of adhesion and plasticity in the peel test. Int. J. Fract. 93, 315–333.

Williams, G.J., 1989. End correction for orthotropic DCB specimen. Comput. Sci. Technol. 35, 367–376.

Williams, G.J., 1995. Fracture in adhesive joints—the beam on elastic foundation model. Proc. ASME Int. Mech. Cong. Exhibit., 1112–1117.

Yang, Q.D., Thouless, M.D., 2001. Mixed mode fracture of plastically-deforming adhesive joints. Int. J. Fract. 110, 175–187.

Yang, Q.D., Thouless, M.D., Ward, S.M., 2000. Analysis of the 90°-peel test with extensive plastic deformation. J. Adhesion 72, 115–132.

Yu, H.H., Hutchinson, J.W., 2002. Influence of substrate compliance on buckling delamination of thin films. Int. J. Fract. 113, 39–55.